The Astronomical Journal, 167:172 (10pp), 2024 April https://doi.org/10.3847/1538-3881/ad2a52
© 2024. The Author(s). Published by the American Astronomical Society.
OPEN ACCESS

Deep Paβ Imaging of the Candidate Accreting Protoplanet AB Aur b

Lauren I. Biddle[1], Brendan P. Bowler[1], Yifan Zhou[2], Kyle Franson[1,4], and Zhoujian Zhang[1,3]
[1] Department of Astronomy, The University of Texas at Austin, 2515 Speedway, Stop C1400, Austin, TX 78712, USA; lbiddle@utexas.edu
[2] Department of Astronomy,University of Virginia, 530 McCormick Road, Charlottesville, VA 22904, USA
[3] Department of Astronomy & Astrophysics, University of California, Santa Cruz, 1156 High Street, Santa Cruz, CA 95064, USA
Received 2023 September 20; revised 2024 February 7; accepted 2024 February 15; published 2024 March 21

Abstract

Giant planets grow by accreting gas through circumplanetary disks, but little is known about the timescale and mechanisms involved in the planet-assembly process because few accreting protoplanets have been discovered. Recent visible and infrared imaging revealed a potential accreting protoplanet within the transition disk around the young intermediate-mass Herbig Ae star, AB Aurigae (AB Aur). Additional imaging in Hα probed for accretion and found agreement between the line-to-continuum flux ratio of the star and companion, raising the possibility that the emission source could be a compact disk feature seen in scattered starlight. We present new deep Keck/NIRC2 high-contrast imaging of AB Aur to characterize emission in Paβ, another accretion tracer less subject to extinction. Our narrow band observations reach a 5σ contrast of 9.6 mag at 0.″6, but we do not detect significant emission at the expected location of the companion, nor from other any other source in the system. Our upper limit on Paβ emission suggests that if AB Aur b is a protoplanet, it is not heavily accreting or accretion is stochastic and was weak during the observations.

Unified Astronomy Thesaurus concepts: Exoplanets (498); Exoplanet formation (492); Direct imaging (387); Protoplanetary disks (1300)

1. Introduction

Direct observations of planetary assembly with high-contrast imaging offers a promising pathway to establish the timescale, location, and mechanisms of giant-planet formation. Planets accrete mass from a circumplanetary disk, which may be continually fed by a circumstellar disk during an embedded phase. Recent modeling efforts have informed observations of planetary-mass-accretion signatures (e.g., Thanathibodee et al. 2019; Aoyama et al. 2020; Szulágyi & Ercolano 2020; Choksi & Chiang 2022; Marleau & Aoyama 2022), predicting increased favorability of detection at wavelengths with strong accretion luminosity, such as line emission from infalling hydrogen gas and excess emission in the UV continuum from accretion hot spots. Ultraviolet (UV) to near-infrared (NIR) imaging of a handful of wide accreting substellar companions show signatures that are consistent with theoretical predictions (e.g., CT Cha B, Schmidt et al. 2008; DH Tau B, Zhou et al. 2014; van Holstein et al. 2021; GQ Lup B, Zhou et al. 2014; Stolker et al. 2021; Demars et al. 2023; GSC 06214-00210 B, Seifahrt et al. 2007; Bowler et al. 2011; Zhou et al. 2014; van Holstein et al. 2021; Demars et al. 2023; SR 12 C, Santamaría-Miranda et al. 2018)—most notably strong Hα and Paβ emission, and relatively bright UV emission.

However, protoplanets still embedded in the circumstellar disk pose a challenge; distinguishing disk substructures, such as concentrated unresolved clumps, from bona fide accreting protoplanets is complex, and many claimed protoplanet candidates identified at thermal wavelengths and in Hα emission have been debated (e.g., LkCa 15 bcd Thalmann et al. 2016; Mendigutía et al. 2018; Currie et al. 2019; HD 100546bc Follette et al. 2017; Rameau et al. 2017; Sissa et al. 2018; HD 169142bc Biller et al. 2014; Pohl et al. 2017; Ligi et al. 2018). PDS 70 b and c (Keppler et al. 2018; Wagner et al. 2018; Haffert et al. 2019) are the only uncontested accreting protoplanets. Recently, visible and infrared imaging revealed a source of concentrated emission in the transition disk surrounding the young (≈4–6 Myr; Guzmán-Díaz et al. 2021; Zhou et al. 2022) accreting A0 star AB Aurigae (Currie et al. 2022), which was interpreted as an embedded protoplanet at a projected separation of 0.″6 (≈100 au). This is near the location where a giant planet was predicted by Tang et al. (2017) via modeling the disk's inner substructure. The source is spatially resolved in multiple data sets and may be tracing circumplanetary disk structure, an envelope, circumstellar disk substructure, or a combination of these.

Protoplanets that are embedded in transition disks are predicted to experience persistent accretion (e.g., Tanigawa et al. 2012; Szulágyi et al. 2014) and will therefore exhibit strong Hα emission from gas that is excited or ionized by intense radiation from the accretion postshock region (Aoyama et al. 2018). If the surrounding envelope is not optically thick, then some or all of this emission will escape. However, the central star in transition disk systems can itself accrete from an inner disk and will also exhibit hydrogen emission. In these cases, the spectrum of a bright unresolved dust feature in the disk seen in scattered light could resemble an accreting planet.

In the case of AB Aur, the host is accreting and shows strong and variable line emission (e.g., Harrington & Kuhn 2007; Costigan et al. 2014). For this reason, confirming the protoplanetary nature of AB Aur b requires careful disambiguation of its own emission from that of surrounding disk features seen in scattered light. Any difference in line strength relative to the continuum between AB Aur A and b would support the hypothesis that AB Aur b is a protoplanet and would point to emission being locally generated. On the

[4] NSF Graduate Research Fellow.

Original content from this work may be used under the terms of the Creative Commons Attribution 4.0 licence. Any further distribution of this work must maintain attribution to the author(s) and the title of the work, journal citation and DOI.

contrary, a consistent line strength would suggest that AB Aur b is actually a compact disk feature seen in scattered starlight.

Zhou et al. (2022) used the Hubble Space Telescope (HST) to search for Hα emission from AB Aur b using narrowband photometry and found that moderate Hα excess is indeed present. In addition, the line-to-continuum ratio of the candidate planet and star are consistent, which calls into question whether the emission originates from planetary accretion or scattered emission. However, the observations were not obtained simultaneously, so the similarity could also be coincidental. New UV and optical HST imaging by Zhou et al. (2023) indicates that at short wavelengths, the emission from AB Aur b is dominated by scattered light from the host star.

If AB Aur b is an accreting planet, then higher-order emission lines such as Paβ should also be present. Paβ is advantageous in searching for distinct accretion signatures from AB Aur b because it is less affected by extinction from the disk in comparison to Hα. In addition, a possible complimentary outcome from a multiwavelength analysis is a constraint on the line-of-sight dust extinction to the source. This could further inform strategies for future imaging of AB Aur b, for instance with the James Webb Space Telescope.

Here, we report the first constraints on Paβ emission from AB Aur b from angular differential imaging (ADI) observations obtained with Keck II/NIRC2. We also characterize the stellar NIR emission line properties of AB Aur with moderate-resolution 0.74–2.50 μm spectroscopy acquired with the NASA Infrared Telescope Facility (IRTF)/SpeX. We outline our observations and data reduction in Section 2. In Section 3, we present the results. See Section 4 for our discussion of the resulting contrast curve and constraint on Paβ line strength. A summary of this work can be found in Section 5.

2. Observations

2.1. Keck II/NIRC2

Adaptive optics images were obtained on UT 2022 September 17 with the NIRC2 camera on the Keck II 10 m Telescope (Wizinowich et al. 2000). The NIRC2 plate scale is 9.971 ± 0.004 mas px^{-1} and the position angle (PA) of each column relative to North is $0\overset{\circ}{.}262 \pm 0\overset{\circ}{.}020$ (Service et al. 2016). Images were acquired in vertical angle mode. We used the central star AB Aur A ($G = 7.11$ mag; Gaia Collaboration 2021) as a natural guide star. The seeing was stable at $\approx 0\overset{''}{.}5$ throughout the observations. All images were read as a centered 512×512 subarray.

We acquired a sequence of 50 images in the Paβ narrowband filter[5] ($\lambda_0 = 1.2903$ μm, $\Delta\lambda = 0.0193$ μm) using ADI (Liu 2004; Marois et al. 2006). The ADI method requires that the telescope pupil remain fixed on the camera while the field of view (FOV) rotates around the star over time. Each image in the ADI sequence was taken with a 1 s integration time and 20 coadds for a total time of 20 s per frame. The total angular rotation of the FOV was $57\overset{\circ}{.}9$, and the total on-source exposure time in Paβ was 16.7 min.

Because AB Aur saturates in the ADI frames, we also captured 25 frames in the Paβ filter with exposure times of 0.2 s, and 100 coadds. AB Aur A was not saturated in these frames, which enabled us to calibrate the contrast of the deep Paβ sequence. In addition, 15 images in the $J_{\rm cont}$ narrowband filter[6] ($\lambda_0 = 1.2132$ μm, $\Delta\lambda = 0.0198$ μm) were obtained with exposure times of 0.3 s. The $J_{\rm cont}$ images allow us to calibrate our measured Paβ emission amplitude of the host star relative to the J-band continuum.

Additional NIRC2 images were taken on UT 2023 May 3 of the A0V standard star HD 109691 to accurately calibrate the AB Aur Paβ line strength for the system throughput response (see Section 3.4). We took two sequences of 10 exposures each in the $J_{\rm cont}$ and Paβ filters with an integration time of 2 s with 1 coadd. A 256×256 subarray was used for both sequences. The average seeing during the observations was $\approx 0\overset{''}{.}5$.

The raw images were cleaned of bad pixels and cosmic rays, then bias subtracted and flat fielded. Optical distortions in the images were corrected with a geometric distortion model for the NIRC2 the narrow field mode characterized by Service et al. (2016). The distortion model was applied to the images using `Rain`,[7] a publicly available Python adaptation of the linear reconstruction software `Drizzle` (Fruchter & Hook 2002). We aligned and median combined the unsaturated frames of AB Aur in Paβ and $J_{\rm cont}$.

2.2. IRTF/SpeX

A moderate-resolution ($R \approx 2000$) NIR spectrum of AB Aur A was acquired from the NASA Infrared Telescope Facility (IRTF) on UT 2022 September 25. We used the SpeX spectrograph (Rayner et al. 2003) in the short-wavelength cross-dispersed (SXD) mode with the $0\overset{''}{.}3 \times 15''$ slit and took 12 exposures with 10 s each in a standard ABBA pattern. The A0V standard star, HD 31069, was observed for telluric correction within an airmass of 0.06 of AB Aur A. We reduced the data using version 4.1 of the Spextool software package[8] (Cushing et al. 2004) and obtained a 0.15 Å dispersion in the wavelength calibration. Our resulting SXD spectrum spans 0.7–2.5 μm, with a signal-to-noise ratio (S/N) of $\approx$440 per pixel near 1.0 μm.

We cataloged the presence and strength of the emission lines in the NIR IRTF SXD spectrum of AB Aur (Figure 1). Many of the hydrogen emission lines occur deep within the line core of a broader absorption feature from the stellar atmosphere, so we compute the equivalent width (EW) only in the wavelength region where the line is in emission, adopting a straight line interpolation of the flux at both endpoints of the emission component as the continuum. In addition to emission from the H I Paschen and Brackett series, we also observe O I, Ca II, and the He I $\lambda 1.0830$ μm line. Table 1 provides identifying information for the prominent emission lines from AB Aur, the observed vacuum wavelength $\lambda_{\rm obs}$, as well as their corresponding EW.

[5] The NIRC2 narrowband Paβ filter transmission profile was digitally extracted from the documentation provided on the NIRC2 instrument page (https://www2.keck.hawaii.edu/inst/nirc2/filters.html). Filter scans were measured at $\approx$300 K, however the NIRC2 operating temperature is $\approx$50 K, resulting in a wavelength offset of the transmission scan. We apply a wavelength correction $\Delta\lambda$ dictated by the thermal expansion properties of the filter: $\Delta\lambda = \alpha \Delta T$ where $\alpha = 2.55 \times 10^{-5}$ μm K^{-1} (R. Campbell 2023, private communication). For $\Delta T = 250$ K, $\Delta\lambda = -0.0064$ μm.

[6] The same correction for the temperature difference between the filter profile scan and the operating temperature was applied to the $J_{\rm cont}$ filter profile as was carried out for Paβ (see footnote 5), except here $\alpha = 3.18 \times 10^{-5}$ μm K^{-1} (R. Campbell 2023, private communication), resulting in a wavelength offset of $\Delta\lambda = -0.0080$ μm.

[7] github.com/jsnguyen/rain developed by Jayke S. Nguyen.

[8] http://irtfweb.ifa.hawaii.edu/~spex/observer/

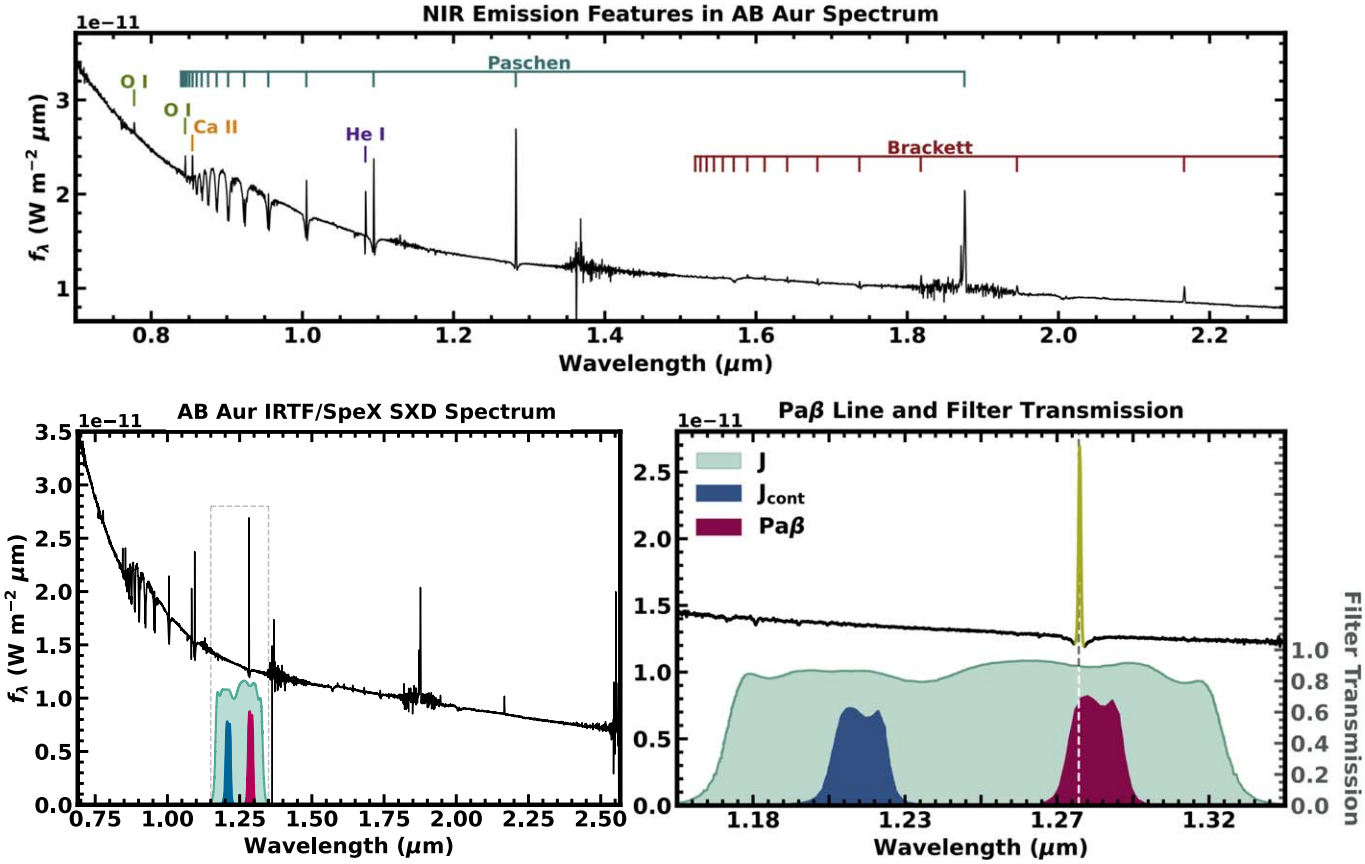


Figure 1. Upper panel: a mapping of the location of emission lines in the NIR IRTF spectrum of AB Aur A. Lower left: the entire flux-calibrated IRTF/SpeX SXD spectrum of AB Aur A (Section 2.2). The spectral ranges ≈1.3–1.5 μm and ≈1.7–1.9 μm fall in telluric regions and have reduced signal to noise. The gray dotted box indicates the spectral region containing the Paβ line and the NIRC2 filter bandpasses utilized in this work. Lower right: a zoomed-in perspective of the region within the dotted box in the left panel. The light-green emission component of the Paβ line indicates the region that was masked during our calculation of the host star's synthetic J_{cont} magnitude ($J_{cont,syn}$). The transmission profiles of the relevant NIRC2 filters are displayed below (*J* filter is shown in teal, the J_{cont} filter is shown in blue, and the Paβ filter is shown in red). The vertical dashed line traces Paβ emission line location.

3. Results

3.1. Point-spread-function Subtraction

We performed point-spread-function (PSF) subtraction on the 50 long-exposure Paβ images from the ADI sequence with `pyKLIP` software[9] (Wang et al. 2015). The KLIP parameters used to produce the PSF-subtracted image were selected according to a data-driven approach inspired by the "pyKLIP Parameter Explorer" algorithm (`pyKLIP-PE`) developed by Adams Redai et al. (2023), whereby the most optimal KLIP parameters are identified based on several image quality metrics describing the effectiveness of PSF subtraction in an injection-recovery analysis. The primary advantage of this data-driven approach is that it ensures the procedure for PSF subtraction does not rely on a prior significant point source detection and reduces cognitive biases in parameter selection (e.g., Follette et al. 2022; Adams Redai et al. 2023).

Our approach aims at optimizing the following parameters that were found by Follette et al. (2022) and Adams Redai et al. (2023) to have the greatest impact on PSF subtraction with `pyKLIP`: `numbasis` (the number of principal components used to construct the PSF), `movement` (the minimum number of pixels through which a planet will have rotated between the target and reference images), and `annuli` (the number of concentric and equal-width annular zones that are analyzed independently by `pyKLIP`).

The procedure for our adopted algorithm is as follows.

1. We first inject several synthetic planets into the preprocessed images at PAs increasing sequentially by 85° and radial separations of one FWHM (4.5 pix, or 0.″044), beginning at a separation of 0.″2 outward to 0.″75. Each synthetic planet is assigned a flux of 7 times the standard deviation of the local image background; a value slightly greater than the 5σ detection threshold, which allows a range of parameter combinations to be tested that will still result in a robust detection.
2. Next, an individual KLIP reduction is performed for every combination of input parameters `numbasis` = [5, 10, 15, 20, 25, 30], `movement` = [1, 2, ..., 24, 25], and `annuli` = [1, 2, ..., 24, 25], probing a range of aggressive and conservative permutations of PSF subtraction. The parameters held constant across all reductions are the inner working angle (`IWA` = 20 pixels), and the number of subsections used to divide the annular zones (`subsections` = 1).
3. Then, the point source detection sensitivity for each combination of parameters is represented as a combination of six quality metrics that are determined based on the recovered properties of the synthetic planets. The quality metrics are:

[9] https://pyklip.readthedocs.io/en/latest/

Table 1
Emission Lines in the IRTF/SpeX NIR Spectrum of AB Aur

Line ID	λ_{obs} (μm)	EW (Å)	σ_{EW} (Å)
O I	0.7776	−0.33	0.06
O I + H I (18–3)	0.8451	−0.62	0.05
Ca II + H I (15–3)	0.8546	−0.97	0.05
H I (14–3)	0.8603	−0.09	0.03
Ca II + H I (13–3)	0.8668	−0.32	0.04
H I (12–3)	0.8754	−0.18	0.03
H I (11–3)	0.8867	−0.36	0.03
H I (10–3)	0.9019	−0.42	0.03
H I (9–3)	0.9233	−0.89	0.04
H I (8–3) Paϵ	0.955	−1.51	0.06
H I (7–3) Paδ	1.0054	−2.96	0.05
He I λ1.0830 μm	1.0837[a]	−2.40	0.06
H I (6–3) Paγ	1.0944	−5.58	0.08
H I (5–3) Paβ	1.2824	−11.58	0.09
H I (19–4)	1.5268	−0.17	0.05
H I (18–4)	1.5349	−0.22	0.05
H I (17–4)	1.5444	−0.24	0.05
H I (16–4)	1.5565	−0.19	0.05
H I (15–4)	1.5708	−0.16	0.04
H I (14–4)	1.5888	−0.42	0.05
H I (13–4)	1.6116	−0.51	0.06
H I (12–4)	1.6414	−0.50	0.06
H I (11–4)	1.6814	−0.62	0.07
H I (10–4)	1.7369	−0.82	0.09
H I (4–3)	1.8759	−21.41	3.71
H I (7–4) Brγ	2.1663	−3.28	0.13

Note.
[a] The He I λ1.0830 μm line exhibits a clear P-Cygni shape, and the reported λ_{obs} signifies the location of the peak of the emission component only.

(a) The average recovered S/N of the injected planets.
(b) The maximum recovered S/N of the injected planets.
(c) The average recovered contrast of the injected planets.
(d) The "false-positive fraction" of the image pixels—the fraction of pixels with a S/N $> 5\,\sigma$ within an annulus at the injected planet's separation with thickness $\Delta r = 5$ pix, or 0.″048 (slightly larger than the FWHM of 4.5 pix, to ensure all necessary pixels are counted). The regions containing the candidate and injected planets are first masked before determining this false-positive fraction.
(e) The final two "neighbor quality" metrics represent the average and maximum S/N metric values listed above. The neighbor quality metrics are obtained by smoothing the average and maximum S/N in `movement/annuli` space for each KL parameter "slice." Neighbor quality metrics are an important consideration because small variations between KLIP parameters should not heavily affect the S/N recovered from a real planet. Smoothing will therefore penalize combinations of `movement` and `annuli` parameters that produce drastic variations in S/N among neighboring cells.

The final selection of `movement` and `annuli`, output metrics that were computed for `numbasis` = 5, and `numbasis` = 30 are averaged, normalized to unity, and summed to produce a single "aggregate quality map" (Figure 2). The cell containing the highest aggregate quality metric (a maximum possible value of 6) yields the combination of `movement` and `annuli` parameters that is optimal, assuming equal weights for each metric in this framework. For this Paβ data set, the best values are `movement` = 4 and `annuli` = 5.

To determine the final `numbasis` component, we repeat this process without averaging any `numbasis` slices, now producing six aggregate quality maps—one for each principle component that we tested. The optimal `numbasis` is that which corresponds to the aggregate quality map with the highest metric corresponding to `movement` = 4 and `annuli` = 5, which we determine to be `numbasis` = 20. Ultimately, the final set of the KLIP parameters that produce the highest quality PSF-subtracted image (Figure 3) is `movement` = 4, `annuli` = 5, and `numbasis` = 20.

3.2. Characterizing Detection Sensitivity in Paβ

We conducted injection-recovery tests to quantify the throughput of the KLIP reduction results and calibrate the 5σ Paβ contrast. Because AB Aur b has been spatially resolved in previous detections (e.g., Currie et al. 2022; Zhou et al. 2023), we perform the injection-recovery test for spatially resolved sources. We also perform the nominal test for unresolved sources to quantify throughput of all potential companions in the field. For both cases, synthetic planets are injected over a series of PAs spaced by 40°, avoiding overlap with the expected PA of AB Aur b (≈180°). For the spatially resolved case, we construct the template of the injected profile by convolving a two-dimensional Gaussian kernel with a FWHM equal to the NIRC2 angular resolution at 1.29 μm (0.″044) with with a flat circle with a radius equal to the intrinsic radius of AB Aur b's spatial profile of ≈0.″045 (Currie et al. 2022). The resulting profile is a spatially extended source with a FWHM = 0.″086.

We injected the spatially extended source at radial separations equally spaced by 2 × FWHM of the injected profile, and each profile was scaled to a peak flux equal to 15 times the standard deviation of the noise within an annulus 1 pixel wide at that planet's separation. These fluxes ensure that the throughput is calculated accurately in postprocessing with minimal effects from artifacts that can be created by bright synthetic planets. The throughput was then computed from the average ratio of the injected and recovered fluxes. Then, the S/N map of the PSF-subtracted image was constructed, first masking out a circular region 2 × FWHM in diameter centered on the expected location of the companion. For each pixel, we measure the flux in an aperture with a diameter equal to twice the FWHM of the PSF. Next, the aperture-integrated flux was divided by the standard deviation of the fluxes in an annulus covering the remaining azimuthal region, producing a map of the S/N for every pixel in the image (Figure 3). We then derived an initial 5σ contrast curve of the postprocessed image by calibrating the deep images with unsaturated Paβ frames. The location of the candidate was masked during this process, and the *t*-distribution correction was applied to account for small number statistics close to the inner working angle (Mawet et al. 2014). The throughput-corrected 5σ contrast curve was computed by dividing the uncorrected contrast value at each resolution element with the throughput at the nearest separation. Figure 4 shows the resulting Paβ contrast achieved at separations out to ≈2.″5 with tabulated values of separation versus Paβ contrast given in Table 2 of the Appendix.

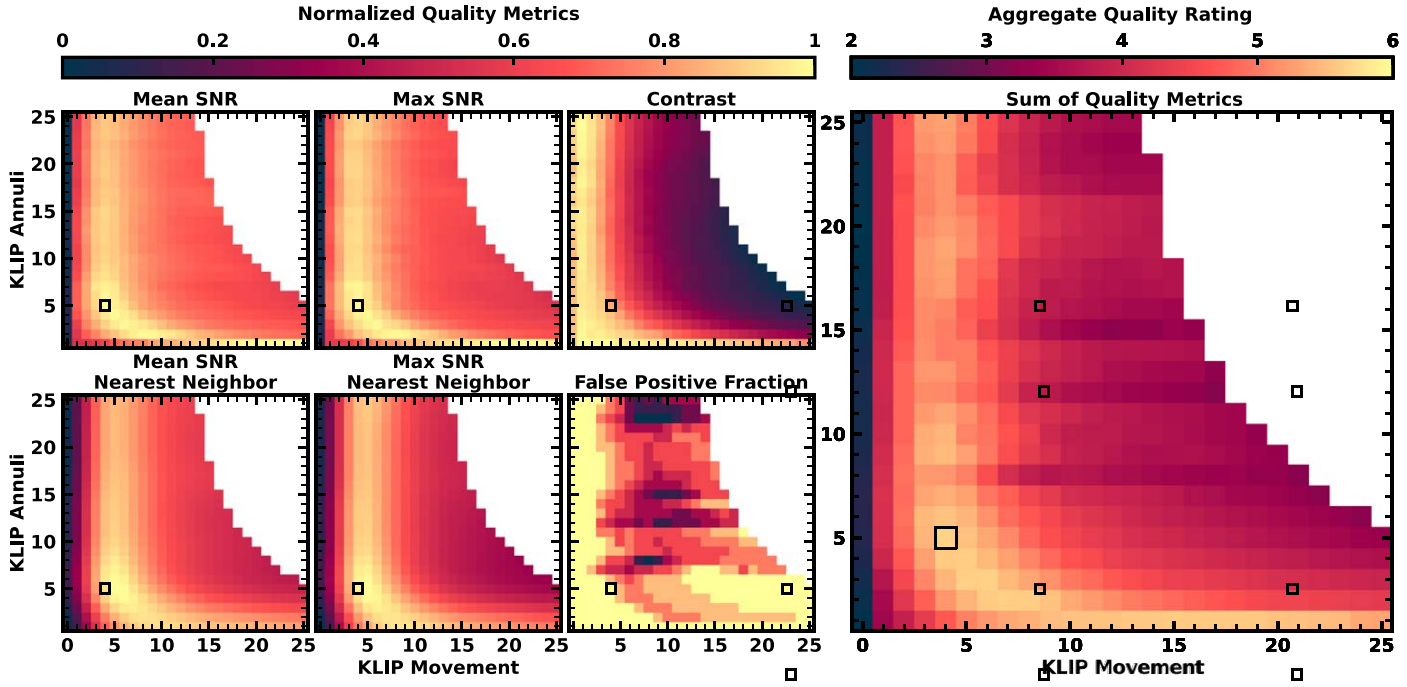


Figure 2. Left six panels: normalized quality maps based on injection-recovery tests for the `movement` and `annuli` parameters of the KLIP processing using 20 principle components. From the upper left to lower right, the metrics presented are: mean S/N, maximum S/N, average contrast, mean S/N nearest neighbor, max S/N nearest neighbor, and false-positive fraction. See Section 3.1 for details. Individual maps are normalized and colored according to the respective quality rating (0 = worst quality, 1 = best quality). These quality metric maps are used to compute the aggregate quality map from which the optimal parameter combinations are chosen. Right panel: the aggregate quality map constructed from the equally weighted summation of all 6 quality metric maps. The cell with the highest rating from the aggregate map is outlined in black in every panel. Cells containing no quality rating have a combination of `movement` and `annuli` parameters that leave no reference images for PSF subtraction as a result of the aggressiveness of the rotational mask.

3.3. No Detection of Paβ Emission

The S/N map of the PSF-subtracted image reveals neither a clear spatially resolved source nor an unresolved source with a S/N ratio at the 5σ detection threshold anywhere in the $2\farcs5 \times 2\farcs5$ FOV surrounding the star. At the expected location of AB Aur b corresponding to the epoch reported by Currie et al. (2022; UT 2020 October 12: sep $= 0\farcs599 \pm 0\farcs005$, PA $= 184\fdg2 \pm 0\fdg6$), the S/N = 1.4. At the location corresponding to the epoch reported by Zhou et al. (2022; UT 2022 March 28: sep $= 0\farcs600 \pm 0\farcs022$, PA $= 182\fdg5 \pm 1\fdg4$), the S/N = 0.8. We therefore do not detect emission in Paβ from AB Aur b. At a separation of $0\farcs6$, the achieved contrast ΔPaβ for a spatially resolved source is 9.6 mag (9.8 mag for an unresolved source). Figure 5 shows four synthetic sources (both resolved and unresolved), injected into the image with fluxes equal to their respective 5σ confidence level with separations $0\farcs4$, $0\farcs6$, $0\farcs8$ and $1\farcs0$ at PA $= 270°$. Each synthetic source is readily visible, and no other comparably bright features are evident elsewhere in the image. Although the continuum contrast between AB Aur b and its host star is lower, $\Delta J \approx 9.2$ mag (Currie et al. 2022), the host star is accreting and exhibits strong emission in Paβ which will impact the contrast in this narrowband filter of the companion, and may explain why the companion was not recovered.

We also note an apparent region of elevated intensity near the expected location of AB Aur b (Figure 3). The region appears to be spatially extended with peak intensity occurring at PA and separation of $184\fdg0$ and $0\farcs55$. The PA is similar to the nominal location of AB Aur b, yet its separation is smaller than the expected separation of the protoplanet. The peak S/N in the region is 4.0, which remains below the 5σ detection threshold. Deeper Paβ observations could help clarify whether this is extended source is real and associated with AB Aur b.

3.4. Monochromatic Paβ Flux Density of AB Aur b

We compute an upper limit on the monochromatic flux density of AB Aur b from the upper limit of the apparent magnitude in Paβ. Typically, this is determined using the apparent magnitude of the central star to calibrate the 5σ contrast achieved at the expected separation of the companion:

$$\mathrm{Pa}\beta_{\mathrm{b}} = \Delta\mathrm{Pa}\beta + \mathrm{Pa}\beta_{\mathrm{A}} \quad (1)$$

where ΔPaβ is the contrast at the separation of the companion, and Paβ_{A} is the apparent magnitude of the host star in Paβ. AB Aur has a strong Paβ emission line, which may vary over time, so the apparent magnitude of the host star in that bandpass during the observations is not known. To recover Paβ_{A} during the long-exposure images used in the high-contrast-imaging sequence, we utilize the following relation,

$$\mathrm{Pa}\beta_{\mathrm{A}} = J_{\mathrm{cont,syn}} - (J_{\mathrm{cont}} - \mathrm{Pa}\beta). \quad (2)$$

Here, $J_{\mathrm{cont,syn}}$ is a synthetic J_{cont} magnitude of AB Aur A, which we derived from our flux-calibrated IRTF spectrum,[10] and the $(J_{\mathrm{cont}} - \mathrm{Pa}\beta)$ color is a single quantity denoting the stellar $J_{\mathrm{cont}} - \mathrm{Pa}\beta$ color measured from the short-exposure (unsaturated) NIRC2 image sequences taken close together in time (within a 10 minutes time frame) immediately prior to the long-exposure ADI sequence. This method for obtaining Paβ_{A}

[10] All synthetic photometry in this work was performed with the `pysynphot` tool set (Lim et al. 2013; https://pysynphot.readthedocs.io/en/latest/).

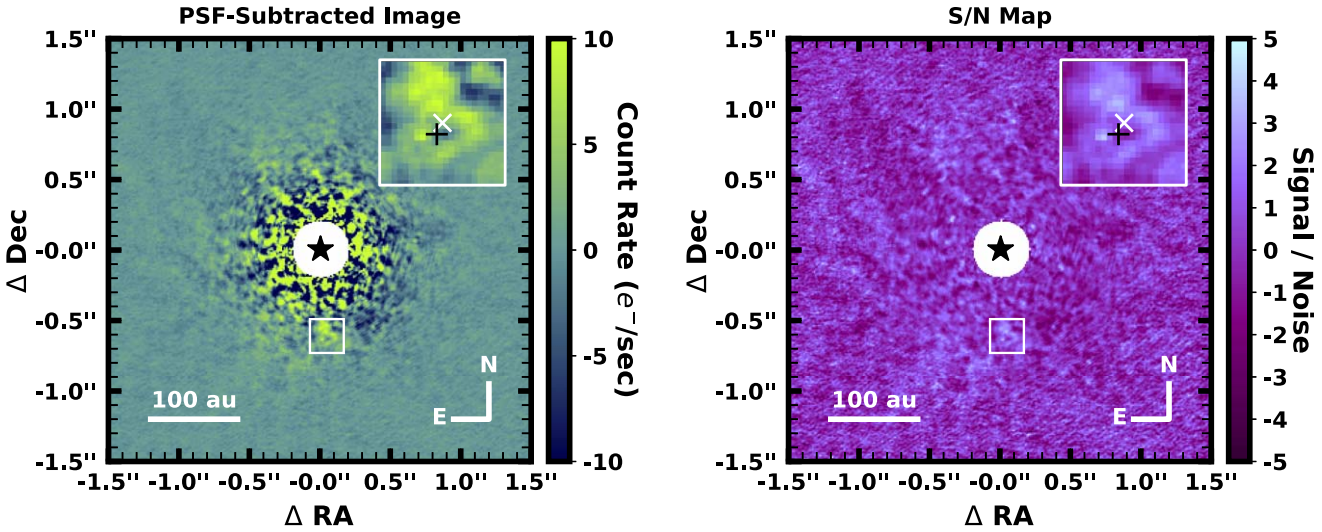


Figure 3. Left: the PSF-subtracted image of AB Aur produced with optimized `pyKLIP` processing parameters (Section 3.1). Right: the S/N map of the PSF-subtracted image where the S/N of each pixel is computed as the flux divided by the standard deviation of the background in a narrow annulus at that pixel's separation. The inset frame in the upper right portion of both panels provides an enlarged perspective of the region outlined by the white box at the expected location of the companion. Within the inset views, the white "×" indicates the most recent location reported by Currie et al. (2022; sep = 0.″60, PA = 184.°2), and the black "+" gives the location reported by Zhou et al. (2022; sep = 0.″60, PA = 182.°5). The S/N within an aperture radius of 3 × FWHM at the position of the white "×" is 1.4, and the S/N at the position of the black "+" is 0.8, both of which are below our threshold of 5σ that we use to establish a reliable detection.

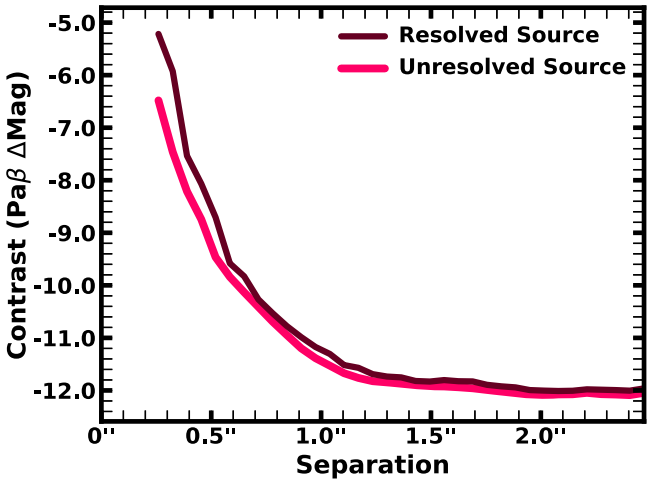


Figure 4. The 5σ contrast curve of the PSF-subtracted image of AB Aur in the NIRC2 narrowband Paβ filter computed for an unresolved source (pink) and a resolved source (maroon). Although the expected ΔJ contrast is ≈9.2 (Currie et al. 2022), the relative Paβ emission line strength between the accreting host star and the candidate companion will impact the contrast of the companion in the Paβ filter.

assumes that AB Aur A's continuum in J is constant. Long-term NIR monitoring by Shenavrin et al. (2019) shows that the J magnitude of the central star varies by 0.37 mag on timescales of ≈1000 days (likely caused by dynamic processes in the inner region of the circumstellar disk; Shenavrin et al. 2019). Furthermore, accretion onto the star could fluctuate, which would vary the emission line strength in the J-band region. For robustness, we adopt this uncertainty into our result for $J_{\rm cont,syn}$.

The IRTF spectrum is flux calibrated by matching the synthetic $J_{\rm MKO}$ filter magnitude to 2MASS J-band photometry (Figure 1). We then performed synthetic photometry using the IRTF spectrum and the NIRC2 $J_{\rm cont}$ filter profile, returning $J_{\rm cont,syn} = 5.96 \pm 0.37$ mag.

Table 2
Separation vs. Paβ Contrast (Figure 4) Achieved in Our High-contrast Imaging of AB Aur

Separation (″)	Spatially Resolved Contrast (Δmag)	Unresolved Contrast (Δmag)
0.26	−5.22	−6.48
0.32	−5.93	−7.46
0.39	−7.54	−8.21
0.45	−8.07	−8.75
0.52	−8.71	−9.46
0.58	−9.58	−9.84
0.65	−9.83	−10.13
0.71	−10.27	−10.41
0.78	−10.53	−10.69
0.84	−10.78	−10.95
0.91	−10.99	−11.2
0.97	−11.17	−11.39
1.04	−11.31	−11.53
1.1	−11.52	−11.67
1.17	−11.57	−11.76
1.23	−11.69	−11.82
1.3	−11.74	−11.85
1.36	−11.75	−11.87
1.43	−11.82	−11.9
1.49	−11.83	−11.91
1.56	−11.8	−11.92
1.62	−11.82	−11.94
1.69	−11.83	−11.96
1.75	−11.89	−12
1.82	−11.92	−12.02
1.88	−11.94	−12.05
1.95	−11.99	−12.08
2.01	−12	−12.09
2.08	−12.01	−12.08
2.14	−12.01	−12.07
2.21	−11.98	−12.05
2.27	−11.99	−12.07
2.34	−11.99	−12.08
2.4	−12	−12.09
2.47	−11.96	−12.05

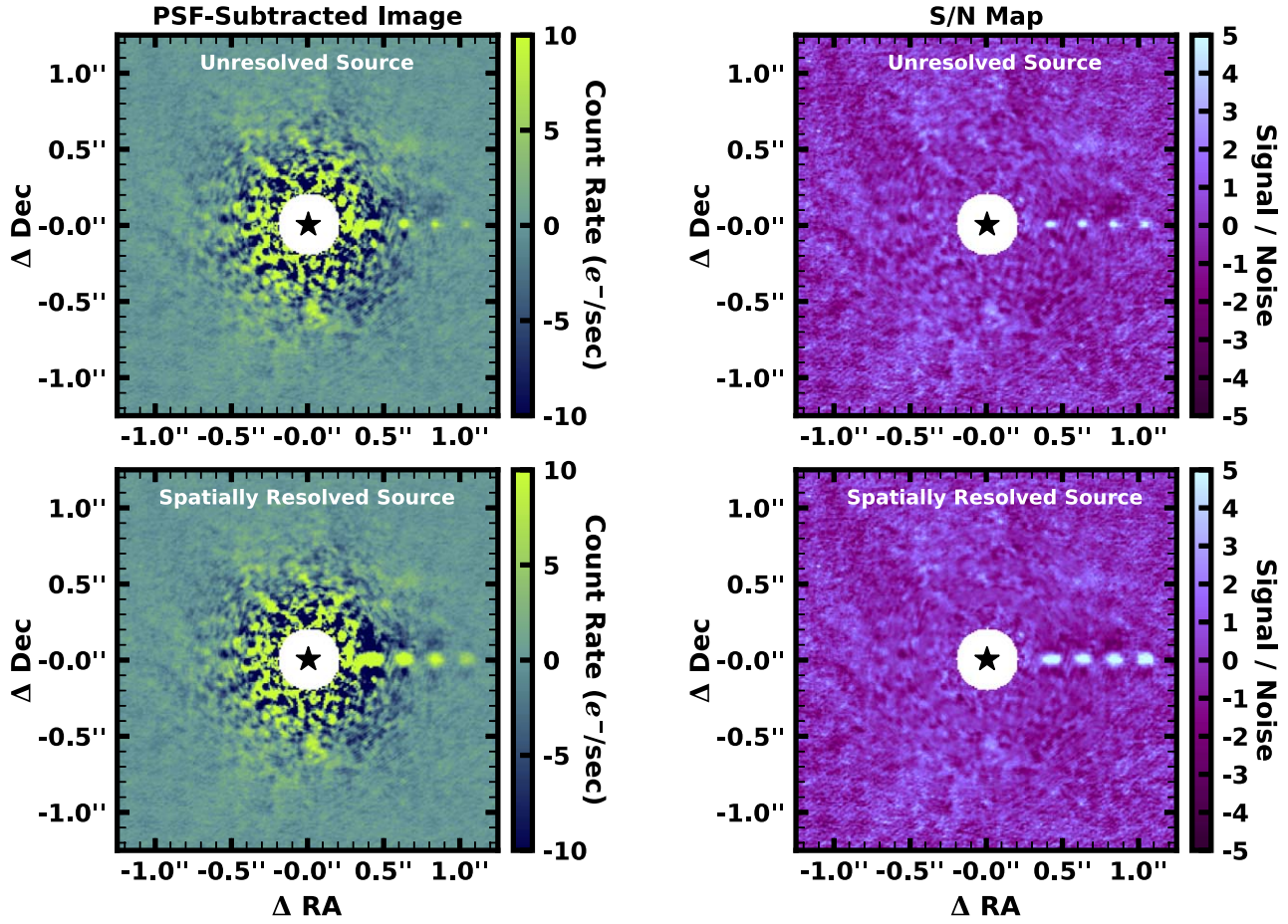


Figure 5. The PSF-subtracted image (left column) and corresponding S/N Map (right column) showing several 5σ injected sources that are unresolved (top row) and spatially resolved (bottom row). The synthetic sources are located at PA = 270° with separations 0.″4, 0.″6, 0.″8, and 1.″0. The FOV is slightly smaller than that in Figure 3 for enhanced visual clarity.

Next, we calculated the $J_{\rm cont} - {\rm Pa}\beta$ color of AB Aur A with the unsaturated $J_{\rm cont}$ and Paβ images. For both filters, the detector counts were summed within a circular aperture centered on the stellar PSF, then divided by the integration times to give count rates in DN s^{-1}. The aperture radius for $J_{\rm cont}$ was $2 \times$ FWHM, and the radius for Paβ was scaled according to the ratio of the central wavelengths of the $J_{\rm cont}$ and Paβ filters.[11] The uncertainty of the total count rate is the standard deviation of that measured for each frame in the associated sequence. This procedure was repeated for the NIRC2 $J_{\rm cont}$ and Paβ images of the A0 star HD 109691 from UT 2023 May 3, which was used to calibrate AB Aur's $J_{\rm cont} - {\rm Pa}\beta$ color to the Vega system as follows:

$$J_{\rm cont} - {\rm Pa}\beta = -2.5 \log_{10} \frac{C_{\rm Jcont}/C_{{\rm Pa}\beta}}{C^{\rm A0}_{\rm Jcont}/C^{\rm A0}_{{\rm Pa}\beta}} \quad (3)$$

where $C_{\rm Jcont}$ and $C_{{\rm Pa}\beta}$ are the measured detector count rates of AB Aur in each filter and $C^{\rm A0}_{\rm Jcont}$ and $C^{\rm A0}_{{\rm Pa}\beta}$ are the count rates measured for an A0 star in each filter. The count ratio $C^{\rm A0}_{\rm Jcont}/C^{\rm A0}_{{\rm Pa}\beta}$ is effectively the color of Vega (or any other A0V star) modulated by wavelength-dependent throughput losses from the atmosphere, telescope, filters, and detector. Using Equation (3), we find a color of $J_{\rm cont} - {\rm Pa}\beta = 0.16 \pm 0.26$ mag.

Using our results for $J_{\rm cont,syn}$ and $J_{\rm cont} - {\rm Pa}\beta$, the Pa$\beta$ apparent magnitude of the star is ${\rm Pa}\beta_{\rm A} = 5.80 \pm 0.44$ mag at the time of our observations. In conjunction with the achieved contrast at 0.″6 separation ($\Delta{\rm Pa}\beta = 9.6$ mag for the resolved case, $\Delta{\rm Pa}\beta = 9.8$ mag for the unresolved case; Section 3.2), the 5σ lower limit on the apparent magnitude of a spatially resolved AB Aur b is ${\rm Pa}\beta_b > 15.40 \pm 0.44$ mag (15.60 ± 0.44 mag for the unresolved scenario). Applying a synthetic Vega Paβ zero-point $f^{\rm Vega}_{{\rm Pa}\beta} = 2.50 \times 10^{-9}$ W m^{-2} μm^{-1}, which was obtained with the Vega spectrum built into `pysynphot`,[12] the associated monochromatic flux density is $f_{{\rm Pa}\beta} \leqslant 1.73 \pm 0.71 \times 10^{-15}$ W m^{-2} μm^{-1} ($1.44 \pm 0.59 \times 10^{-15}$ W m^{-2} μm^{-1}, unresolved). We proceed with a conservative treatment of $f_{{\rm Pa}\beta}$, and adopt a hard upper limit equal to 2σ above the mean value: henceforth, $f_{{\rm Pa}\beta} \leqslant 3.14 \times 10^{-15}$ W m^{-2} μm^{-1} (2.61×10^{-15} W m^{-2} μm^{-1}, unresolved; Figure 6).

[11] While this takes into account the slight difference in aperture radius between the $J_{\rm cont}$ ($\lambda_0 = 1.2132$) and Paβ ($\lambda_0 = 1.2903$) filters, so as to preserve the same fractional energy in the PSF, we have assumed a constant Strehl ratio in both filters.

[12] https://pysynphot.readthedocs.io/en/latest/spectrum.html#pysynphot-vega-spec

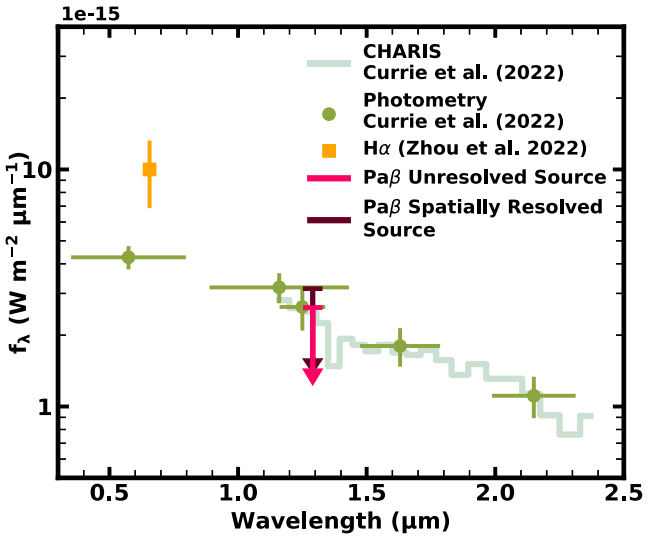


Figure 6. SED of AB Aur b. The adopted upper limit of the flux density in Paβ for an unresolved source is indicated by the pink downward-pointing arrow, whereas the upper limit of the flux density for a spatially resolved source is shown depicted as a maroon arrow. The green circles are the optical (HST) and NIR (Subaru) photometry reported by Currie et al. (2022), and the CHARIS spectrum they report is represented in light-green. The orange square point indicates the Hα excess identified by Zhou et al. (2022) with HST.

3.5. Paβ Equivalent Width

To estimate the central star's EW at the time of imaging, we masked the Paβ emission line flux in the IRTF/SpeX SXD spectrum, and replaced the missing flux with a series of artificial emission lines with amplitudes ranging from -1 to 14 times the flux of the continuum at the line center, increasing sequentially by factors of 0.1. Each line is assigned a width corresponding to the SXD resolving power of $\approx$0.0006 μm. Next, the EW is calculated individually for each line and then mapped to the synthetic stellar $J_{\rm cont} - {\rm Pa}\beta$ derived from the IRTF spectrum containing the corresponding simulated emission line. The true EW of the stellar Paβ emission line is then inferred from the simulated $J_{\rm cont} - {\rm Pa}\beta$ color that matches the observed value ($J_{\rm cont} - {\rm Pa}\beta = 0.16 \pm 0.26$ mag; Figure 7). The results of this test indicate that the EW of the stellar Paβ line at the time of the imaging sequence is –94 $\pm$ 64 Å. The EW of the Paβ emission line in the IRTF spectrum obtained $\sim$8 days later is -11.58 ± 0.09 Å (Table 1).

We obtained the companion's maximum detectable Paβ emission line strength with similar methods. We injected synthetic emission line profiles are into the CHARIS NIR spectrum of AB Aur b from Currie et al. (2022) following the same prescription for line amplitude and width as was done for the central star. The EW of each simulated emission line was mapped to the corresponding flux density of the continuum-plus-emission line through the NIRC2 Paβ filter. Using this empirical relationship between Paβ flux density and EW (Figure 7), we determine that AB Aur b's flux density upper limit $f_{{\rm Pa}\beta} \leqslant 3.14 \times 10^{-15}$ W m^{-2} μm^{-1} (2.61×10^{-15} W m^{-2} μm^{-1}, unresolved) corresponds to a lower[13] limit in its EW of –54 Å (–11 Å, unresolved). A significant difference in strength of the Paβ emission line between the star and the companion would be evidence that the companion is self-luminous (i.e., a protoplanet). However, their

[13] Noting that the EW for emission lines is negative, so weaker emission would yield higher values that are lower in magnitude.

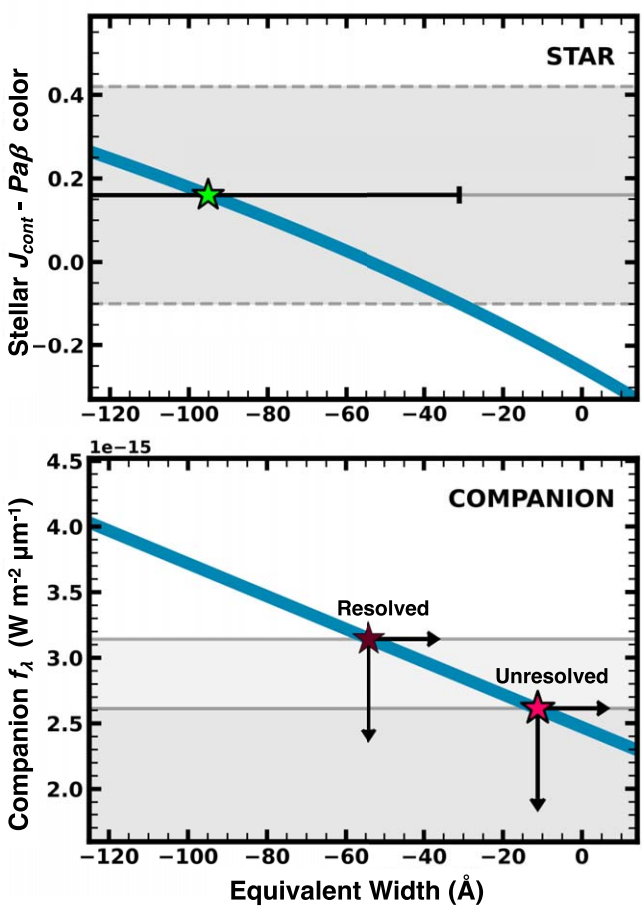


Figure 7. EWs and stellar color and companion flux density corresponding to simulated Paβ emission lines injected into the stellar continuum (top) and companion continuum (bottom). The solid gray line in the top panel indicates the real measured stellar $J_{\rm cont} - {\rm Pa}\beta$ and the shaded region bounded by dashed lines represents the 1σ uncertainty on the measurement. The green star marks the simulated quantity that matches the observed stellar $J_{\rm cont} - {\rm Pa}\beta$. The bottom panel shows the EW estimations for both an unresolved source and spatially resolved source. The uppermost boundary of each of the shaded regions indicates the upper limit of the companion flux density determined in Section 3.4. The pink and maroon stars mark the simulated quantities that match the measured upper limits on the companion's flux density if it were unresolved or resolved, respectively. EW values are negative for emission lines.

EWs agree at the 0.64σ and 1.3σ level for the spatially resolved and unresolved cases, respectively, offering no evidence of a significant ($\geqslant 3\sigma$) discrepancy in Paβ emission. This is consistent with both the light-scattering scenario as well as the scenario in which a young planet is weakly accreting.

4. Discussion

Our deep Paβ imaging does not reveal excess emission from AB Aur b, nor any other point source in the system. There is some tension between our upper limits at the location of the planet and the nominal published J-band continuum level of AB Aur b. As described in Section 3.4, the 5σ contrast level corresponds to an upper limit of $1.73 \pm 0.71 \times 10^{-15}$ W m^{-2} μm^{-1} assuming a spatially resolved source (or $1.44 \pm 0.59 \times 10^{-15}$ W m^{-2} μm^{-1} for the unresolved case in which AB Aur b is a point source), which is below the continuum emission reported by Currie et al. (2022) at this wavelength. But as there is an uncertainty associated

with our upper limit, we have conservatively adopted the 95% upper bound on this value to guard against potential systematic errors in the multistep process of converting contrast measurements into a flux density within this narrowband filter.

There are a few potential explanations that can account for the companion flux being undetectable at the published continuum level.

1. If we consider the companion to be a self-luminous protoplanet, we can rule out strong Paβ emission, implying weak accretion or no accretion at all from the companion.
2. Alternatively, if the companion's emission source is a compact protoplanetary disk feature seen in scattered starlight, one or both of the following may be possible. The localized dynamics in the disk material could have changed the effective light-scattering area of the disk substructure (e.g., LkCa 15 Thalmann et al. 2016; Currie et al. 2019; Sallum et al. 2023). Alternatively, there could have been enhanced Paβ emission caused by accretion onto the central star, but the delay in light travel time to reach the companion may have prevented the observation of enhanced emission at the location of AB Aur b within the observing window.
3. Finally, irrespective of the true nature of the emission source, the following two possibilities could also contribute to this modest tension: the *J*-band region is known to be moderately variable at the 0.4 mag level (Shenavrin et al. 2019), and could have affected the continuum flux calibration (see also Section 3.4).
4. Alternatively, the absolute calibration level of the CHARIS continuum may be inaccurate. For this analysis, we have assumed that the companion's continuum is both constant and accurate.

5. Summary

In this work, we obtained high-contrast imaging of AB Aur with Keck/NIRC2 in the Paβ narrowband filter. We do not detect significant Paβ emission in the FOV surrounding the star, either from AB Aur b or any other potential embedded planets. However, the depth of our observations place a meaningful upper limit on the Paβ line flux. Mapping this flux to its associated EW, we find that, if present, Paβ emission is weak. However, we cannot conclude whether it must be significantly weaker in comparison to emission from the central star at the time of the observations, which would have provided a direct test of the scattered light versus self-luminous hypothesis because the line-to-continuum ratio is expected to differ in the latter scenario. Deeper Paβ imaging, NIR spectroscopy, and multiwavelength observations of AB Aur b will help clarify the nature of this enigmatic source.

Acknowledgments

We extend our gratitude to the anonymous referee for their thoughtful and constructive feedback. We also thank the staff at Keck Observatory for their assistance in enabling these observations and their execution. B.P.B. acknowledges support from the National Science Foundation grant AST-1909209, NASA Exoplanet Research Program grant 20-XRP20_2-0119, and the Alfred P. Sloan Foundation. This work made use of the following software: `Astropy` (Robitaille et al. 2021), `Numpy` (Van Der Walt et al. 2011), `Scipy` (Virtanen et al. 2021), `Matplotlib` (Hunter 2007), `pyKLIP` (Wang et al. 2015), and `pysynphot` (Lim et al. 2013).

Appendix
Paβ Contrast Curve

Here we provide the contrast curves achieved in our high-contrast imaging of AB Aur. In Table 2 we tabulate the contrast corresponding to each separation for the spatially resolved and unresolved cases.

ORCID iDs

Lauren I. Biddle https://orcid.org/0000-0003-2646-3727
Brendan P. Bowler https://orcid.org/0000-0003-2649-2288
Yifan Zhou https://orcid.org/0000-0003-2969-6040
Kyle Franson https://orcid.org/0000-0003-4557-414X
Zhoujian Zhang https://orcid.org/0000-0002-3726-4881

References

Adams Redai, J. I., Follette, K. B., Wang, J., et al. 2023, AJ, 165, 57
Aoyama, Y., Ikoma, M., & Tanigawa, T. 2018, ApJ, 866, 84
Aoyama, Y., Marleau, G.-D., Mordasini, C., & Ikoma, M. 2020, arXiv:2011.06608
Biller, B. A., Males, J., Rodigas, T., et al. 2014, ApJL, 792, L22
Bowler, B. P., Liu, M. C., Kraus, A. L., Mann, A. W., & Ireland, M. J. 2011, ApJ, 743, 148
Choksi, N., & Chiang, E. 2022, MNRAS, 510, 1657
Costigan, G., Vink, J. S., Scholz, A., Ray, T., & Testi, L. 2014, MNRAS, 440, 3444
Currie, T., Lawson, K., Schneider, G., et al. 2022, NatAs, 6, 751
Currie, T., Marois, C., Cieza, L., et al. 2019, ApJL, 877, L3
Cushing, M. C., Vacca, W. D., & Rayner, J. T. 2004, PASP, 116, 362
Demars, D., Bonnefoy, M., Dougados, C., et al. 2023, A&A, 676, A123
Follette, K. B., Close, L. M., Males, J. R., et al. 2022, AJ, 165, 45
Follette, K. B., Rameau, J., Dong, R., et al. 2017, AJ, 153, 264
Fruchter, A. S., & Hook, R. N. 2002, PASP, 114, 144
Gaia Collaboration 2021, A&A, 649, 20, I/350
Guzmán-Díaz, J., Mendigutía, I., Montesinos, B., et al. 2021, A&A, 650, A182
Haffert, S. Y., Bohn, A. J., de Boer, J., et al. 2019, NatAs, 3, 749
Harrington, D. M., & Kuhn, J. R. 2007, ApJL, 667, L89
Hunter, J. D. 2007, CSE, 9, 90
Keppler, M., Benisty, M., Müller, A., et al. 2018, A&A, 617, A44
Ligi, R., Vigan, A., Gratton, R., et al. 2018, MNRAS, 473, 1774
Lim, P. L., Diaz, R. I., & Laidler, V., 2013 pysynphot: Synthetic Photometry Software Package, Astrophysics Source Code Library, ascl:1303.023
Liu, M. C. 2004, Sci, 305, 1442
Marleau, G.-D., & Aoyama, Y. 2022, RNAAS, 6, 262
Marois, C., Lafrenière, D., Doyon, R., Macintosh, B., & Nadeau, D. 2006, ApJ, 641, 556
Mawet, D., Milli, J., Wahhaj, Z., et al. 2014, ApJ, 792, 97
Mendigutía, I., Oudmaijer, R. D., Schneider, P. C., et al. 2018, A&A, 618, L9
Pohl, A., Benisty, M., Pinilla, P., et al. 2017, ApJ, 850, 52
Rameau, J., Follette, K. B., Pueyo, L., et al. 2017, AJ, 153, 244
Rayner, J. T., Toomey, D. W., Onaka, P. M., et al. 2003, PASP, 115, 362
Robitaille, T., Tollerud, E., Aldcroft, T., et al. 2021, astropy/astropy: v4.2.1, Zenodo, doi:10.5281/zenodo.4670729
Sallum, S., Eisner, J., Skemer, A., & Murray-Clay, R. 2023, ApJ, 953, 55
Santamaría-Miranda, A., Cáceres, C., Schreiber, M. R., et al. 2018, MNRAS, 475, 2994
Schmidt, T. O. B., Neuhäuser, R., Seifahrt, A., et al. 2008, A&A, 491, 311
Seifahrt, A., Neuhäuser, R., & Hauschildt, P. H. 2007, A&A, 463, 309
Service, M., Lu, J. R., Campbell, R., et al. 2016, PASP, 128, 095004
Shenavrin, V. I., Grinin, V. P., Baluev, R. V., & Demidova, T. V. 2019, ARep, 63, 1035
Sissa, E., Gratton, R., Garufi, A., et al. 2018, A&A, 619, A160
Stolker, T., Haffert, S. Y., Kesseli, A. Y., et al. 2021, AJ, 162, 286
Szulágyi, J., & Ercolano, B. 2020, ApJ, 902, 126
Szulágyi, J., Morbidelli, A., Crida, A., & Masset, F. 2014, ApJ, 782, 65
Tang, Y.-W., Guilloteau, S., Dutrey, A., et al. 2017, ApJ, 840, 32
Tanigawa, T., Ohtsuki, K., & Machida, M. N. 2012, ApJ, 747, 47

Thalmann, C., Janson, M., Garufi, A., et al. 2016, ApJL, 828, L17
Thanathibodee, T., Calvet, N., Bae, J., Muzerolle, J., & Hernández, R. F. 2019, ApJ, 885, 94
Van Der Walt, S., Colbert, S. C., & Varoquaux, G. 2011, CSE, 13, 22
van Holstein, R. G., Stolker, T., Jensen-Clem, R., et al. 2021, A&A, 647, A21
Virtanen, P., Gommers, R., Burovski, E., et al. 2021, scipy/scipy: SciPy v1.6.3, Zenodo, doi:10.5281/zenodo.4718897
Wagner, K., Follete, K. B., Close, L. M., et al. 2018, ApJL, 863, L8
Wang, J. J., Ruffio, J.-B., De Rosa, R. J., et al., 2015 pyKLIP: PSF Subtraction for Exoplanets and Disks, Astrophysics Source Code Library, ascl:1506.001
Wizinowich, P., Acton, D. S., Shelton, C., et al. 2000, PASP, 112, 315
Zhou, Y., Bowler, B. P., Yang, H., et al. 2023, AJ, 166, 220
Zhou, Y., Herczeg, G. J., Kraus, A. L., Metchev, S., & Cruz, K. L. 2014, ApJL, 783, L17
Zhou, Y., Sanghi, A., Bowler, B. P., et al. 2022, ApJL, 934, L13